Aggregate

WILEY

Aggregate Open Access

RESEARCH ARTICLE OPEN ACCESS

Plasmon-Doped Organic Heterojunction Optoelectronic Synapses for Near-Infrared Visual Memory and Neuromorphic Computing

Jiangcheng Cao[1] | Hong Lian[1,2,3] | Xianglin Wang[1] | Qishuai Huang[4] | Jiahui Ding[1] | Jiangnan Xia[3] | Shuanglong Wang[3] | Weijin Hu[4,5] | Tom Wu[3] | Qingchen Dong[1,2]

[1]MOE Key Laboratory of Advanced Display and System Applications, Shanghai University, Shanghai, People's Republic of China | [2]School of Mechanical & Electronic Engineering and Automation, Shanghai University, Shanghai, People's Republic of China | [3]Department of Applied Physics, The Hong Kong Polytechnic University, Hong Kong SAR, People's Republic of China | [4]Shenyang National Laboratory For Materials Science, Institute of Metal Research, Chinese Academy of Sciences, Shenyang, People's Republic of China | [5]School of Materials Science and Engineering, University of Science and Technology of China, Shenyang, People's Republic of China

Correspondence: Hong Lian (hlian@polyu.edu.hk) | Shuanglong Wang (shuanglong.wang@polyu.edu.hk) | Tom Wu (tom-tao.wu@polyu.edu.hk) | Qingchen Dong (qcdong@shu.edu.cn)

Received: 17 December 2025 | **Revised:** 9 February 2026 | **Accepted:** 24 February 2026

Keywords: gold nanorods (AuNRs) | organic optoelectronic synapses | localized surface plasmon resonance (LSPR) | near-infrared (NIR) light | neuromorphic computing

ABSTRACT

The explosive growth of artificial intelligence has intensified demands for new computing paradigms beyond conventional von Neumann architectures. In response, brain-inspired computing-in-memory technologies are emerging as a promising path forward. Here, we designed a two-terminal optical synaptic device utilizing organic heterojunctions doped with gold nanorods (AuNRs), leveraging the electric field enhancement innate to the localized surface plasmon resonance (LSPR) effect. The device doped with 1 wt% AuNRs demonstrates a markedly enhanced light absorption capacity in the near-infrared (NIR) region of 808 nm. The generation rate of photogenerated excitons increases by 16.8%, while the probability of exciton dissociation rises by 8.4%. The paired-pulse facilitation (PPF) index reaches 114.6% ($\Delta t = 1$ s), indicating heightened sensitivity to optical pulse parameters. Additionally, Hall effect measurements were performed to characterize the electrical properties of the PEDOT:PSS:AuNRs films. The carrier mobility of the doped films increased 20-fold compared to pristine PEDOT:PSS due to electron injection from AuNRs. This enhanced mobility contributes to faster synaptic response and higher conductance tunability in the synapse device, further supporting its performance in neuromorphic computing tasks. Furthermore, we successfully simulated the dynamic "learning–forgetting–relearning" processes associated with human visual memory. By exploiting the tunable conductance of the optimized synaptic device, we implemented both convolutional neural networks (CNNs) and convolutional spiking neural networks (CSNNs) for weight updates. After 100 and 150 training epochs, the system achieved recognition accuracies up to 98.57% for handwritten digits and 92.01% for dynamic gestures. This work presents an effective plasmon-doping approach to enhancing the performance of organic memristors and can be extended to other material systems.

Jiangcheng Cao and Hong Lian contributed equally to this work.

This is an open access article under the terms of the Creative Commons Attribution License, which permits use, distribution and reproduction in any medium, provided the original work is properly cited.

© 2026 The Author(s). *Aggregate* published by SCUT, AIEI, and John Wiley & Sons Australia, Ltd.

Aggregate, 2026; 7:e70319
https://doi.org/10.1002/agt2.70319

1 | Introduction

With the continuous evolution of AI technology across various application fields, including intelligent manufacturing, smart cities, healthcare, and autonomous driving, the demand for computing power is experiencing exponential growth [1]. Traditional silicon chips based on the von Neumann architecture suffer from the physical separation of memory and processing units, leading to frequent data transfers that consume over 90% of time and energy, and are no longer able to meet the ever-increasing demands for computational power and energy efficiency [2, 3]. Biologically inspired strategies like neuromorphic computing enable parallel information processing, offering a promising route to overcome these bottlenecks [4, 5]. In the human brain, the visual system—responsible for sensing and preliminarily processing optical signals—accounts for over 80% of sensory information input [6]. Optoelectronic synaptic devices are capable of efficiently integrating optoelectronic signal sensing, processing, and memory functionalities [7–12]. Moreover, these devices are susceptible to both optical stimulation and voltage signals, thereby enhancing computational speed while simultaneously minimizing crosstalk and energy consumption [13–17]. Near-infrared (NIR) light, with its strong penetration, biocompatibility, low power consumption, and resistance to interference in dark or complex environments, plays a crucial role in applications such as night surveillance, optical communication, data encryption, physiological monitoring, and medical imaging. Notably, neuromorphic chips based on NIR-responsive photoelectric synapses offer significant advantages for sensor-computing integration in brain–computer interfaces and biomedical applications [18–21].

However, most photoelectric synaptic devices to date rely on inorganic semiconductors, which, due to their intrinsic bandgap limitations, typically exhibit high sensitivity only within the visible spectrum, while showing poor or negligible response to NIR light. This spectral constraint leads to high power consumption and compromised long-term stability, limiting their applicability in NIR-related scenarios [22–29]. Furthermore, inhibitory postsynaptic currents (IPSCs) within inorganic optoelectronic synapses are typically induced through electrical pulses or by modulating the polarity and amplitude of the voltage, which complicates artificial neural network (ANN) algorithms, further leading to additional energy expenditure [30, 31]. Additionally, inorganic semiconductor synaptic devices generally employ a three-terminal transistor structure, which not only entails a complicated fabrication process with elevated costs but also suffers from limited mechanical flexibility and biocompatibility. The degree of integration for the transistors is also approaching the physical limit, making it increasingly difficult to satisfy the growing practical demands associated with artificial intelligence applications.

Organic optoelectronic synaptic devices intrinsically possess several advantageous characteristics, including structural tunability, adjustable electronic bandgaps, solution processability, mechanical flexibility, and superior biocompatibility. Furthermore, the two-terminal memristor-type photoelectric synapses based on organic semiconductors exhibit structural and operational similarities to biological synapses, facilitating their integration with microprocessor cores on-chip. Among organic optoelectronic synaptic devices, those based on photovoltaic-type bulk heterojunction (BHJ) structures exhibit enhanced photoelectric performance owing to their large interfacial areas and abundant defect sites, which facilitate efficient exciton generation and dissociation [32, 33]. Leveraging these structural advantages enables the construction of analog memristors with improved light response, suppressed dark current, and reduced power consumption, thereby advancing high-performance optical synaptic learning, memory emulation, and neuromorphic computing [34–37]. Currently, research on optoelectronic synapses utilizing organic BHJ is still in its early stage. There are limited reports regarding reconfigurable devices that exhibit excellent spectral response capabilities in the NIR region. In 2025, our group made a pioneering contribution by reporting a flexible two-terminal memristor based on the PM6:L8-BO active layer [38]. This device successfully demonstrated long-term potentiation (LTP) and long-term depression (LTD) under full NIR light excitation. Additionally, we constructed an artificial reflection arc using this synaptic device, achieving the complete operational chain encompassing perception, storage, processing, and execution within a simulated biological system.

In this work, to further enhance NIR light responsivity and reduce the power consumption of BHJ organic photonic synapses (BHJ-OPSs), gold nanorods (AuNRs) with strong localized surface plasmon resonance (LSPR) effect were incorporated into the electron-blocking layer (EBL), enabling the realization of a two-terminal BHJ-OPS device with significantly improved NIR photoresponse. Compared to the control device, the AuNRs-doped device demonstrates higher excitatory postsynaptic current (EPSC) and paired-pulse facilitation (PPF) index under NIR pulsed light excitation. Additionally, it exhibits more pronounced synaptic behaviors such as spike number-dependent plasticity (SNDP), spike time width-dependent plasticity (STDP), and spike intensity-dependent plasticity (SIDP). Hall effect measurements show that AuNRs doping boosts carrier mobility and switches conduction from p- to n-type, enhancing exciton dissociation and transport, which together with plasmon-enhanced absorption improves overall synaptic performance. Furthermore, these plasmon-doped devices display exceptional adaptability and reconfigurability, with a single-synaptic event power consumption as low as 4.5 fJ. Spectral analysis, morphological characterization, and theoretical simulations reveal that doping AuNRs into the PEDOT:PSS layer induces a strong LSPR effect in the NIR region, significantly boosting exciton generation and dissociation efficiency, thereby enhancing overall synaptic performance. Based on the excellent photonic synaptic performance of the AuNRs-doped BHJ-OPS, brain-inspired processes such as memory retention and forgetting were emulated. The conductance states of the light-tunable devices were mapped to a convolutional neural network (CNN) and a convolutional spiking neural network (CSNN) for weight updates, enabling high-accuracy recognition of static handwritten digits (98.57%) and dynamic gestures (92%). This work offers a promising strategy for constructing fully light-controlled, NIR-responsive reconfigurable OPS in neuromorphic computing.

2 | Results and Discussion

Figure 1a presents a schematic diagram illustrating the operational process of the human eye in perceiving external visual

26924560, 2026, 3, Downloaded from https://onlinelibrary.wiley.com/doi/10.1002/agt2.70319 by HONG KONG POLYTECHNIC UNIVERSITY HU NG HOM, Wiley Online Library on [10/04/2026]. See the Terms and Conditions (https://onlinelibrary.wiley.com/terms-and-conditions) on Wiley Online Library for rules of use; OA articles are governed by the applicable Creative Commons License

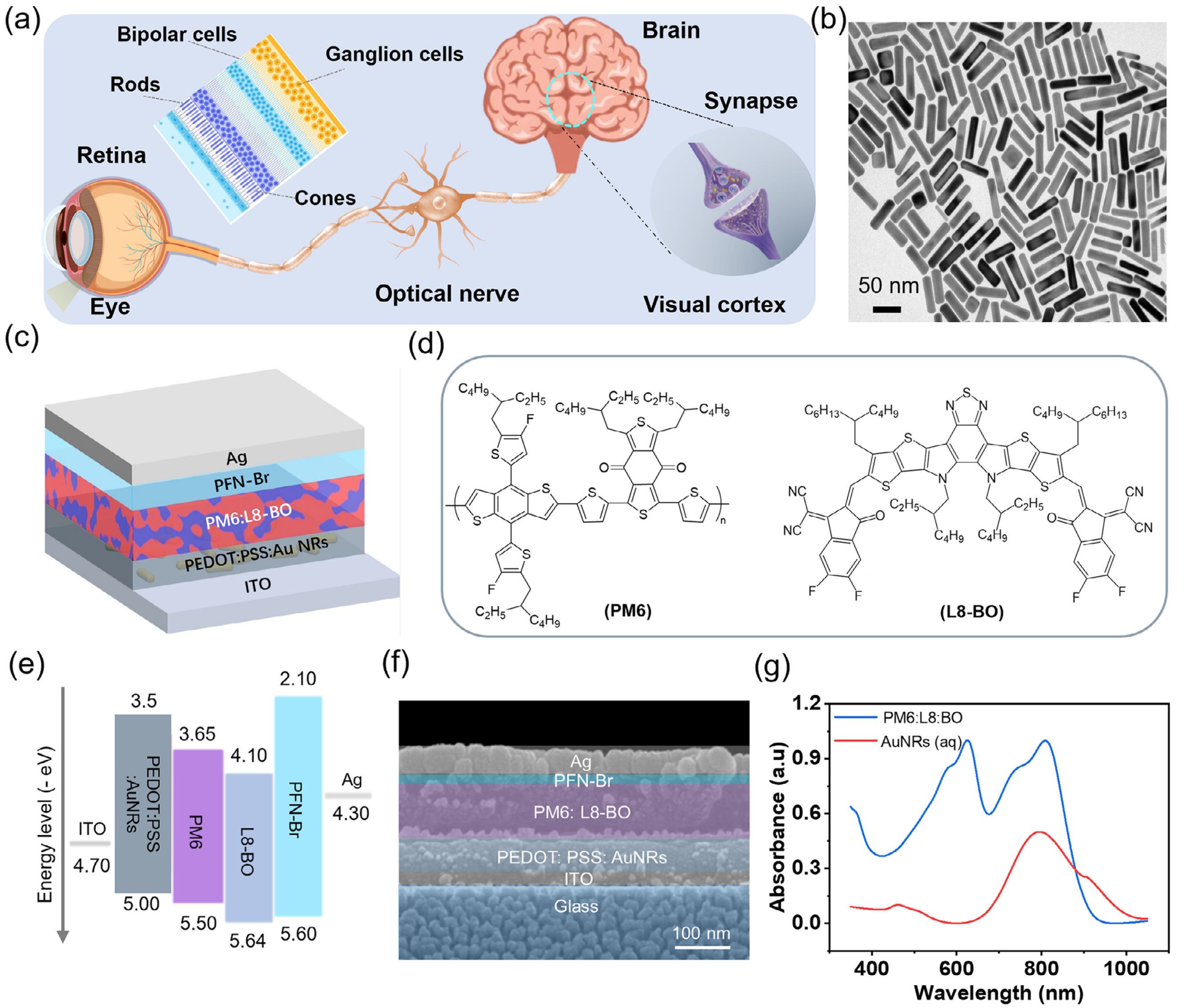

FIGURE 1 | (a) Schematic of the human visual system. (b) TEM image of as-prepared AuNRs. (c) The device configuration of the doped device: ITO/PEDOT:PSS:AuNRs/PM6:L8-BO/PFN-Br/Ag. (d) The chemical structures of the donor (PM6) and acceptor (L8-BO) materials as used in the BHJ-OPS device. (e) Energy level diagram of the doped BHJ-OPS device. (f) Cross-sectional SEM image of the doped BHJ-OPS device. (g) UV-vis-NIR absorption spectra of PM6:L8-BO film and the AuNRs aqueous solution, respectively.

information. When external light is focused onto the retina through the refractive lens, the photoreceptor cells located on the retina, specifically cone cells (responsible for bright and color vision) and rod cells (responsible for dim light vision), convert photons into neural electrical signals [39, 40]. Subsequently, bipolar cells directly receive signals from photoreceptor cells and transmit them to ganglion cells. In addition, amacrine cells connect bipolar and ganglion cells laterally, contributing to dynamic signal processing such as motion detection. Ultimately, the axons of ganglion cells converge to form the optic nerve, which transmits visual signals to the brain's visual cortex for final processing and formation of visual perception. Synapses serve as critical nodes facilitating precise transmission, modulation, integration, and computation of visual signals between neurons. They significantly influence both processing efficiency and perceptual quality of visual information [41, 42]. Recently, it has been recognized that the two-terminal memristor-type photonic synapses exhibit structural and functional similarities to biological synapses and can be seamlessly integrated on-chip with microprocessor cores [43].

To improve the NIR synaptic performance of OPSs, we focus on the design and synthesis of AuNRs with LSPR extinction wavelengths extending beyond 800 nm. To achieve this, finite element method (FEM) simulations were first conducted to explore how the LSPR extinction wavelength correlates with the structural dimensions of the AuNRs, offering guidance for precise LSPR tuning. Figure S1a presents the contour plot of the LSPR extinction wavelength as a function of AuNRs width and length. Figure S1b shows the extinction spectrum of AuNRs with a length of 65 nm and a diameter (width) of 15 nm. The results confirm that adjusting the AuNRs' geometry can effectively modulate the LSPR extinction wavelength in the NIR regime, promising to enhance the performance of OPSs. Figure 1b presents a

26924560, 2026, 3, Downloaded from https://onlinelibrary.wiley.com/doi/10.1002/agt2.70319 by HONG KONG POLYTECHNIC UNIVERSITY HU NG HOM, Wiley Online Library on [10/04/2026]. See the Terms and Conditions (https://onlinelibrary.wiley.com/terms-and-conditions) on Wiley Online Library for rules of use; OA articles are governed by the applicable Creative Commons License

transmission electron microscopy (TEM) image of our prepared AuNRs, revealing a uniform nanorod-like morphology with an average length of 65.26 ± 6.75 nm and an average width of 14.60 ± 1.94 nm, respectively (see Figure S2), matching well with the simulation configuration.

Figure 1c illustrates the device configuration featuring ITO as the transparent anode, PEDOT:PSS or PEDOT:PSS:AuNRs as the EBL, and PFN-Br as the hole-blocking layer (HBL). The active layer is composed of PM6 (donor):L8-BO (non-fullerene acceptor), with their molecular structures shown in Figure 1d. The energy level diagram of the device is depicted in Figure 1e, illustrating a cascade alignment of the functional materials that enhances light responsivity while maintaining synaptic characteristics. Figure 1f displays a cross-sectional scanning electron microscopy (SEM) image of the BHJ-OPS device, clearly distinguishing the functional layers. Furthermore, as shown in Figure 1g, the ultraviolet–visible–near-infrared (UV-vis-NIR) absorption spectrum reveals that the PM6:L8-BO blend film exhibits complementary absorption over the wavelength range of 380–1000 nm (Figure S3). In addition, the aqueous solution of AuNRs exhibits strong absorption in the wavelength range of 650–1050 nm [44, 45]. When 1 wt% AuNRs were incorporated into PEEDOT:PSS, the resulting PEEDOT:PSS:AuNRs/PM6:L8-BO film demonstrates a significantly enhanced NIR light absorption performance compared to the undoped film. This would have a substantial impact on the NIR synaptic performance of the AuNRs-doped BHJ-OPSs.

We investigated how varying the AuNRs concentration affects synaptic performance. Figure S4a,b displays the EPSC and PPF results for undoped, 0.5%, 1%, and 2% doped devices triggered by 808 nm optical pulses (0.51 mW cm^{-2}, 5 s pulse width). Among these, the device with 1% AuNRs content exhibited superior performance, characterized by the highest initial EPSC and the most prolonged decay time. Regarding short-term plasticity, although the PPF index inversely correlated with pulse interval (Δt) across all groups, the 1% doped device maintained a maximum PPF index of 114.3% ($\Delta t = 1$ s), surpassing the 110.8% observed in the undoped counterpart. These results underscore the critical role of AuNRs in boosting synaptic functionality. Therefore, the 1% AuNRs concentration was selected as the optimal condition for the remaining experiments and applications. Initially, by measuring the light and dark currents of an undoped and 1% doped device, we determined that the built-in potentials for the doped and undoped devices are 0.3 V and 0.5 V, respectively, as illustrated in Figure 2a and Figure S5a. This result indicates a decreased operating voltage in the doped device, suggesting enhanced photoresponsive ability and demonstrating its potential advantages in synaptic plasticity. Moreover, we measured the carrier mobility of both PEDOT:PSS and PEDOT:PSS:AuNRs films using Hall measurements (Figure 2a inset), calculated by $\mu = \frac{|R_{\mathrm{H}}|}{\rho}$(where R_{H} is the Hall coefficient, and ρ is resistivity). We found that the mobility of PEDOT:PSS:AuNRs (20.8 cm^2 V^{-1} s^{-1}) is significantly higher than that of the pristine PEDOT:PSS film (1.0 cm^2 V^{-1} s^{-1}), indicating that the incorporation of AuNRs can enhance the carrier transport capability of the devices, which is consistent with the single-carrier results, as shown in Figure S6. This may be because the AuNRs form conductive pathways within the PEDOT:PSS matrix, which facilitates carrier transport. The detailed procedures and results are provided in Tables S1 and S2, and Figures S10 and S11. Notably, the pristine PEDOT:PSS film is p-type, while the AuNRs-doped film exhibits n-type character, as evidenced by their opposite Hall voltages, which we attribute to electron doping from the AuNRs. Figure 2b and Figure S5b present the I–V curves of the doped device and control device obtained over 10 repeated cycles under 808 nm light pulses at a bias voltage of 0.8 V. The control device exhibits a smaller memory window and unstable memristive behavior. In contrast, the doped device shows a gradual increase in conductivity over successive dual forward sweeps, indicating a stable and reliable light-triggered synaptic response. Furthermore, the device exhibited a distinct hysteresis window, indicating reversible resistive switching behavior. Notably, 10 clearly distinguishable resistance states were identified, highlighting the device's potential for multi-level memory storage and synaptic weight modulation in neuromorphic systems.

To further explore how effectively the doped device responds to light at different wavelengths, we then employed pulsed light sources at wavelengths of 380 and 525 nm (0.51 mW cm^{-2}, 1 s pulse width) as excitation stimuli, respectively, as shown in Figure S7a,b. Figure 2c compares the variations in the device's conductance states under these three illumination conditions. It is evident that the device exhibits hysteresis windows and resistive switching behavior under all three wavelengths. Notably, under 808 nm illumination, the resistive switching behavior is the most pronounced, with 10 well-distinguished conductance states, indicating a particularly strong photoresponse to NIR light. This enhancement is primarily attributed to robust LSPR effects exhibited by AuNRs within NIR regions, which markedly improve their responsiveness toward such wavelengths. To explore the influence of AuNRs doping on the EPSC response, devices were subjected to pulsed light stimuli at 380, 525, and 808 nm (0.51 mW cm^{-2}, 1 s pulse width). As illustrated in Figure S8 and Figure 2d, the EPSC triggered by 808 nm illumination was markedly stronger than those induced by 380 and 525 nm light. Notably, the device doped with 1% AuNRs exhibited a significant enhancement in EPSC under 808 nm stimulation compared to the control device, indicating the effectiveness of AuNRs incorporation in boosting NIR synaptic performance.

Synaptic plasticity plays a crucial role in computational processes, memory retention, and learning functions within biological nervous systems. The PPF index is a typical measure of short-term plasticity (STP), which refers to the accumulation of carriers generated when a second light pulse excites a device while residual carriers from an initial pulse remain active, thereby eliciting a heightened EPSC response (as depicted in Figure 2e). PPF can be calculated using Formula (1) [46]:

$$\mathrm{PPF} = (A_2/A_1) \times 100(\%) \tag{1}$$

Here, A_1 and A_2 represent postsynaptic currents (PSCs) following the first and second pulse stimuli, respectively. PPF is directly influenced by both time intervals and pulse frequencies between consecutive stimuli. Reducing the interval Δt between two successive pulses—or conversely increasing their frequency—will result in either an increase or decrease in PPF or synaptic weights.

26924560, 2026, 3, Downloaded from https://onlinelibrary.wiley.com/doi/10.1002/agt2.70319 by HONG KONG POLYTECHNIC UNIVERSITY HU NG HOM, Wiley Online Library on [10/04/2026]. See the Terms and Conditions (https://onlinelibrary.wiley.com/terms-and-conditions) on Wiley Online Library for rules of use; OA articles are governed by the applicable Creative Commons License

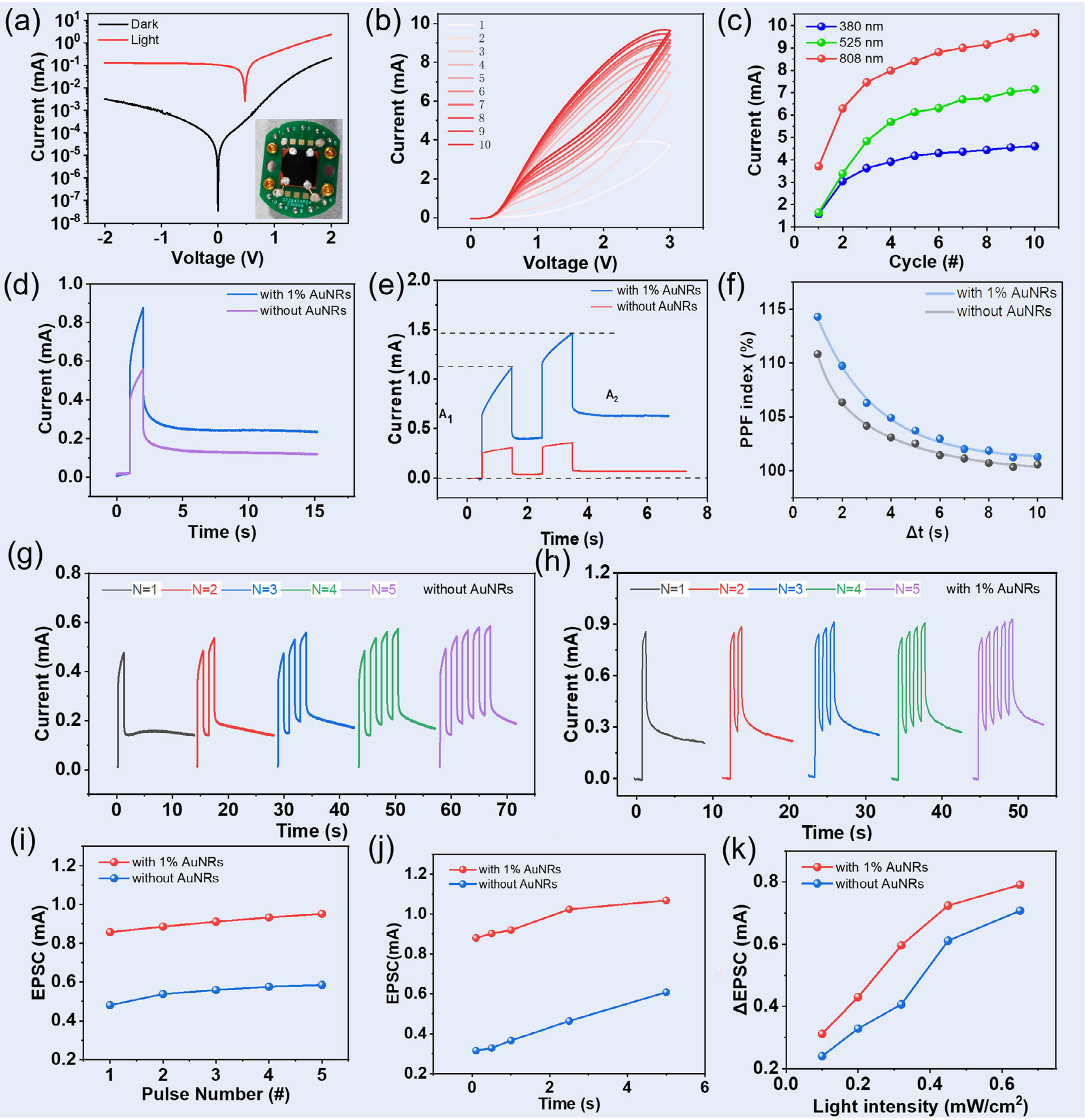

FIGURE 2 | (a) *I–V* characteristic curves of the doped BHJ-OPS device under light and dark conditions (inset: the real device connection image). (b) The *I–V* curves of the doped BHJ-OPS device after 10 consecutive dual positive voltage sweeps under 808 nm light illumination. (c) Variations in conductance states of the doped BHJ-OPS device under illumination of 380, 525, and 808 nm, respectively. (d) The EPSC of doped and undoped BHJ-OPS devices. (e) EPSC stimulated by two continuous 808 nm light spikes for doped and undoped BHJ-OPS devices. (f) The PPF index of doped and undoped BHJ-OPS devices, resulting from light pulses (1 mW cm^{-2}, 1 s pulse width) at a wavelength of 808 nm, respectively, plotted against Δ*t*. EPSC curves of (g) undoped BHJ-OPS devices and (h) doped BHJ-OPS device under different number of 808 nm light pulses. The effects of (i) pulse numbers, (j) pulse widths, and (k) intensities of 808 nm light pulses on the EPSC change values (Δ_{EPSCs}) of BHJ-OPS devices, respectively.

When there is minimal temporal separation between identical stimuli, memory strength within neural circuits tends to enhance. Conversely, longer intervals correlate with diminished memory retention and increased likelihood of forgetting [47]. The PPF index of the doped and undoped devices exhibits a gradual decline as the interval Δ*t* extends from 1 to 10 s, as illustrated in Figure 2f. This decay behavior can be well described by a double-exponential fitting model, expressed as follows:

$$\mathrm{PPF} = C_1 \exp - \frac{\Delta t}{\tau_1} + C_2 \exp - \frac{\Delta t}{\tau_2} \qquad (2)$$

where τ_1 and τ_2 denote the relaxation time constants corresponding to the fast and slow decay components, respectively.

26924560, 2026, 3, Downloaded from https://onlinelibrary.wiley.com/doi/10.1002/agt2.70319 by HONG KONG POLYTECHNIC UNIVERSITY HU NG HOM, Wiley Online Library on [10/04/2026]. See the Terms and Conditions (https://onlinelibrary.wiley.com/terms-and-conditions) on Wiley Online Library for rules of use; OA articles are governed by the applicable Creative Commons License

It can be observed that when Δt equals 1 s, the PPF index for the device containing AuNRs measures at 114.6%, notably surpassing that of the control device at 111.8%. Furthermore, as Δt increases, both doped and undoped devices exhibit a gradual decline in their respective PPF indices. This indicates that doping with AuNRs can significantly enhance the optical response and synaptic performance of the device. The PSC of the device can be effectively modulated by varying the number, duration, and intensity of light pulses. Figure 2g,h illustrates the SNDP for both undoped and doped devices, demonstrating that the EPSC increases as the number of pulses rises from 1 to 5. Specifically, for the undoped device, PSC increased from 0.476 to 0.577 mA, while for the doped device, it rose from 0.520 mA to a higher value of 0.674 mA, indicating a more substantial increase. Moreover, as depicted in Figure S9, synaptic plasticity can be modulated by tuning the width and intensity of the presynaptic light pulses. Figure 2i–k further depicts how plasticity varies with respect to the number, width, and intensity of light pulses for both undoped and doped devices. It is evident that as these parameters increase—namely pulse number, width, and intensity—the PSC progressively rises. Notably, this increase is more pronounced in the doped device compared to its undoped counterpart. These findings strongly support that doped devices exhibit superior NIR light responsiveness. Consequently, the AuNRs-doped BHJ-OPS demonstrates enhanced plasticity, which will translate into improved neuromorphic perception capabilities in the artificial vision system.

Individuals tend to forget certain information they have learned over time. During the process of relearning, they typically require less time to re-acquire previously forgotten information, while simultaneously enhancing their memory retention. To simulate this biological learning process, we employed the doped device to mimic empirical learning behavior (Figure 3a). As illustrated in Figure 3b, during the initial training stage, the EPSC of the device significantly increased upon continuous application of 30 light pulses. Following the cessation of light pulse stimulation, a gradual attenuation process resembling memory decay was observed over a period of approximately 30 s (short-term memory [STM]). In contrast, during the second training stimulus, only 13 consecutive light pulses were necessary to achieve an equivalent PSC level that was attained after the first training session—substantially fewer than the 30 light pulses required initially. Furthermore, the rate at which current decayed (indicative of forgetting) was slower in this instance (57 s), thereby demonstrating the efficacy of empirical learning (long-term memory [LTM]) [48]. To further investigate differential responses under continuous light stimulation, we applied 10 consecutive 808 nm light pulses and successfully obtained 10 distinct conductance states (Figure 3c), indicating that the device possesses multilevel storage capabilities when subjected to optical stimuli.

Additionally, we discovered that these devices exhibit neuromorphic characteristics akin to those found in human irises: upon applying a series of 1 Hz pulsed lights at a wavelength of 808 nm to the AuNRs-doped BHJ-OPS device, we noted an initial increase in PSC; however, after approximately 65 pulses had been administered, there was a gradual decline in PSC levels (Figure 3d). This phenomenon parallels how biological irises regulate incoming light flux by adjusting pupil size in response to intense illumination—thereby preventing retinal damage. Such adaptability highlights the potential of a doped device to maintain robust performance and enable accurate perception even in complex environments [49]. To further evaluate retention over extended timescales, we monitored the conductance states over 12 h under ambient conditions, as shown in Figure 3e. The devices exhibit a slow and gradual conductance decay rather than abrupt failure, indicating intrinsically stable memory states. The dominant retention-loss mechanism is attributed to the gradual relaxation of trapped charges at the interfacial states within the BHJ and at the electrode/organic interfaces. This charge detrapping process occurs over long timescales and is commonly observed in organic synaptic and memory devices. Importantly, no irreversible degradation or sudden conductance collapse was observed, suggesting that the memory loss is governed by reversible charge trapping and detrapping processes rather than chemical or structural damage. This indicates that the doped device possesses excellent LTM retention capability. As depicted in Figure 3f, reversible potentiation and depression behaviors were reliably triggered by alternately applying 25 optical pulses at 808 nm (1 mW cm^{-2}, 1 s) and 25 pulses at 1060 nm (10 mW cm^{-2}, 1 s). Moreover, even under repeated LTP/LTD cycles applied to randomly chosen devices, the output current exhibited minimal variation with increasing cycle number. These findings collectively confirm that the all-optically driven synaptic plasticity can be stably and repeatably modulated, underscoring the strong reproducibility of the doped devices. To demonstrate the repeatable reliability of the BHJ-OPS in practical applications, device-to-device and cycle-to-cycle variations for five devices have been further tested, as shown in Figure S12. Furthermore, when multiple LTP/LTD cycles are applied to the randomly selected device using repeated light pulses, the current shows only a negligible change, even as the number of cycles increases. All the above results demonstrate that the all-optically induced LTP and LTD can be operated stably and repeatably, indicating the excellent reproducibility of our BHJ-OPS. Although minor variations are observed, which can be attributed to fabrication-induced inhomogeneity of devices, the overall synaptic behaviors and modulation trends remain highly consistent across devices. The energy consumption per synaptic event (E) is a key metric for assessing the efficiency of photonic synaptic devices [50]. It was estimated using the following equation:

$$E = I \times \Delta t \times V \tag{3}$$

Here, I represents the peak EPSC, Δt denotes the pulse duration, and V is the applied voltage. As shown in Figure 3g, when a low voltage of 0.5 V was applied with a pulse duration of 1 ms, a discernible EPSC of 8.9×10^{-12} A was still generated. This results in an ultra-low energy consumption of just 4.5 fJ per event—outperforming the energy efficiency of natural biological synapses [51]. As summarized in Table 1, the proposed NIR synaptic device shows competitive performance in terms of energy efficiency, response speed, array scale, and task accuracy compared with previously reported NIR synaptic systems. From these results, it is evident that the doped BHJ-OPS device exhibits favorable synaptic plasticity along with robust long-term retention characteristics. Additionally, it showcases light-controlled reconfigurability and sensitivity to weak light stimuli. These attributes confer significant advantages for spatiotemporal information fusion applications, making it suitable for use in

26924560, 2026, 3, Downloaded from https://onlinelibrary.wiley.com/doi/10.1002/agt2.70319 by HONG KONG POLYTECHNIC UNIVERSITY HU NG HOM, Wiley Online Library on [10/04/2026]. See the Terms and Conditions (https://onlinelibrary.wiley.com/terms-and-conditions) on Wiley Online Library for rules of use; OA articles are governed by the applicable Creative Commons License

TABLE 1 | Performance of devices based on different structures and materials.

Device	Wavelength	Energy consumption	Response Time	Responsivity	Endurance	PPF index	NL	Array size	Accuracy	Ref
In_2Se_3/MoS_2	490–1060 nm	28 fJ (1060 nm)	—	—	—	111.6 %	—	10 × 10	—	[53]
IGZO/Perovskite QDs	635–405 nm	500 fJ (635 nm)	—	—	—	278 %	—	7 × 7	>90 %	[54]
ReS_2	450–808 nm	12.12 fJ (808 nm)	—	—	—	124 %	—	—	97%	[55]
$PMMA/MoSe_2/Bi_2Se_3$	700–850 nm	100 pJ (790 nm)	—	—	1000	—	—	—	—	[56]
ZnAlSnO/SnO	405, 532, 635 nm	0.75 pJ (635 nm)	—	—	—	169 %	—	—	91.40%	[57]
$CsPbBr_2I/P3HT$	445–980 nm	—	60 ms	—	—	117.5 %	—	—	85.63%	[58]
InAs NW	750–1550 nm	—	160 ms	839.3 A/W	—	160 %	—	—	—	[59]
$(PEA)_2SnI_4$	470–660 nm	—	50 ms	—	—	129.7%	—	—	—	[60]
Si-NC	375–1342 nm	—	200 ms	—	—	119 %	—	—	94 %	[61]
$SrTiO_3:(Y_2O_3:ZrO_2)$	405–650 nm		—	1.6 A/W	10^8	117.5 %	—	—	91.5%	[62]
$MoTe_2/BaTiO_3$	450/520/650 nm	41.2 pJ (450 nm)	—	—	10000	120 %	—	—	91.73% 97.50%	[63]
$Zr\text{-}CsPbI_3$	650–405 nm	—	—	—	2500	—	—	—	68.3%	[27]
Ga_2O_3/MoS_2	365 nm	—	—	—	8000	140 %	—	—	—	[64]
$CuSbS_2$	808 nm	—	—	—	200	190 %	—	—	92.3%	[65]
InGaAs	760 nm	—	—	34.59 A/W	—	—	—	16 × 16	82%	[66]
ZnSe/InP:Cu	405–790 nm	—	—	70.5 A/W	—	550 %	—	3 × 3	—	[67]
$MoSe_2$	240–1700 nm	10 fJ (1060 nm)	—	—	—	128 %	—	10 × 10	—	[68]
WSe_2/h-BN	415 nm	—	—	—	—	138 %	0.31 (−80 V)/−2.2 (+ 80 V)	—	93.11 %	[69]
IGZO/SnO/SnS	266, 405, 520, 658 nm	—	—	—	—	112.5 %	1.72 (266 nm)/−3.07 (405, 520, 658 nm)	8 × 8	91%	[70]
CuPc/p-6P	655, 450, 365 nm	—	—	—	—	—	0.01 (365 nm)/−4.6 (−10 V)	—	87.11%	[71]
$HfS_2/HfO_x/SnS_2$	365, 532, 820 nm	—	—	—	—	150 %	0.22(−60 V)/−1.88 (60 V)	—	90 %	[72]
WSe_2	532 nm, X-ray	—	—	—	—	—	0.61 (3 V)/−3.15 (−1 V)	—	93.75%	[73]
PM6:L8-BO	808 nm	4.5 fJ (808 nm)	2 ms	5.95 A/W	10,000	114.6%	0.62 (808 nm)/−0.43 (1060 nm)	26 × 26	98.57% 92.01%	This Work

26924560, 2026, 3, Downloaded from https://onlinelibrary.wiley.com/doi/10.1002/agt2.70319 by HONG KONG POLYTECHNIC UNIVERSITY HU NG HOM, Wiley Online Library on [10/04/2026]. See the Terms and Conditions (https://onlinelibrary.wiley.com/terms-and-conditions) on Wiley Online Library for rules of use; OA articles are governed by the applicable Creative Commons License

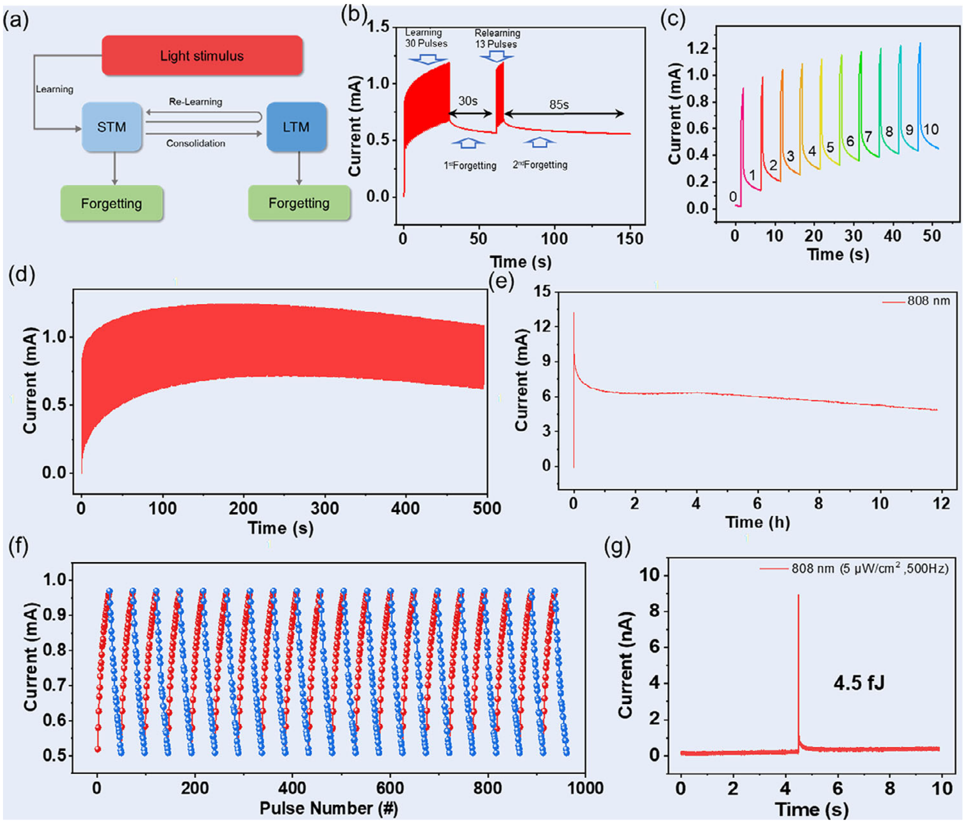

FIGURE 3 | (a) Schematic of the transformation from STM to LTM in the human brain. (b) Learning experience behavior was emulated using two sequential 808 nm light pulse training stimulations. (c) Multistate behaviors of the doped BHJ-OPS device under 10 consecutive light stimulations. (d) Adaptive behavior of the doped BHJ-OPS device under continuous light pulses. (e) LTP behavior triggered by NIR light pulses (808 nm, 10 pulses). (f) Cyclic LTP/LTD curves of the doped BHJ-OPS device for the memory and forgetting process. (g) Ultralow energy consumption was measured at $V = 0.5$ V with stimulation of 808 nm light pulse of 5 μW cm^{-2} for 2 ms.

object recognition, enhancement tasks, and motion perception within autonomous vehicles and monitoring systems [52].

The spatial distributions of the electric field intensity in OPS with AuNRs embedded in the EBL, were investigated through FEM simulations. As shown in Figure 4a,b, the electric field distribution under 820 nm light excitation—near the LSPR peak of the AuNRs—exhibits a pronounced near-field enhancement around the AuNRs, particularly at their tips, with the enhanced field extending into the active layer. These AuNRs exhibit nanoantenna-like behavior, effectively increasing the optical path length of incoming photons via scattering mechanisms, which subsequently enhances light absorption within the active layer [74]. To further understand the role of AuNRs in absorption improvement, the time-averaged Poynting vector was computed using the following expression [75]:

$$\vec{\Pi}\left(\vec{r},\omega\right) = \frac{1}{2}\vec{E}\left(\vec{r},\omega\right) \times \vec{H}\left(\vec{r},\omega\right) \tag{4}$$

Here, $\vec{H}$ denotes the magnetic field. The vector $\vec{\pi}$, representing the time-averaged Poynting vector, was evaluated along the white-dashed ellipsoids and red lines, as illustrated in Figure 4b. These elements mark the positions where the extremities of the Poynting vectors originate from the ellipsoidal contours. The simulation result reveals that the scattered light propagates predominantly perpendicular to the induced dipoles and is strongly directed forward—into the active layer—following the path of the incident light. This forward-directed scattering becomes especially prominent in the NIR region, aligning with the longitudinal dipolar plasmon mode. Besides, the Poynting vector reflects the direction and intensity of electromagnetic energy flow, highlighting the enhanced NIR absorption within the active layer attributable to the inclusion of AuNRs. These findings are consistent with experimental observations. The results indicate that the local enhancement of the electric field near AuNRs is the primary driving factor for increased NIR absorption, facilitated through the synergistic effects of LSPR, light scattering, and their mutual interaction. This improved absorption promotes greater exciton generation, thereby enhancing EPSC and extended retention time.

To elucidate the influence of AuNRs doping on film morphology and its correlation with optoelectronic performance, atomic force microscopy (AFM) measurements were conducted on ITO/PEDOT:PSS/PM6:L8-BO and ITO/PEDOT:PSS:AuNRs/PM6:L8-BO films, as shown in Figure 4c,d. The root-mean-square (RMS) roughness (R_q) of the AuNRs-doped film was measured to be 1.46 nm, which is comparable to that of the pristine film (1.30 nm), indicating that the incorporation of AuNRs does not significantly perturb the surface morphology. This suggests that the AuNRs

26924560, 2026, 3, Downloaded from https://onlinelibrary.wiley.com/doi/10.1002/agt2.70319 by HONG KONG POLYTECHNIC UNIVERSITY HU NG HOM, Wiley Online Library on [10/04/2026]. See the Terms and Conditions (https://onlinelibrary.wiley.com/terms-and-conditions) on Wiley Online Library for rules of use; OA articles are governed by the applicable Creative Commons License

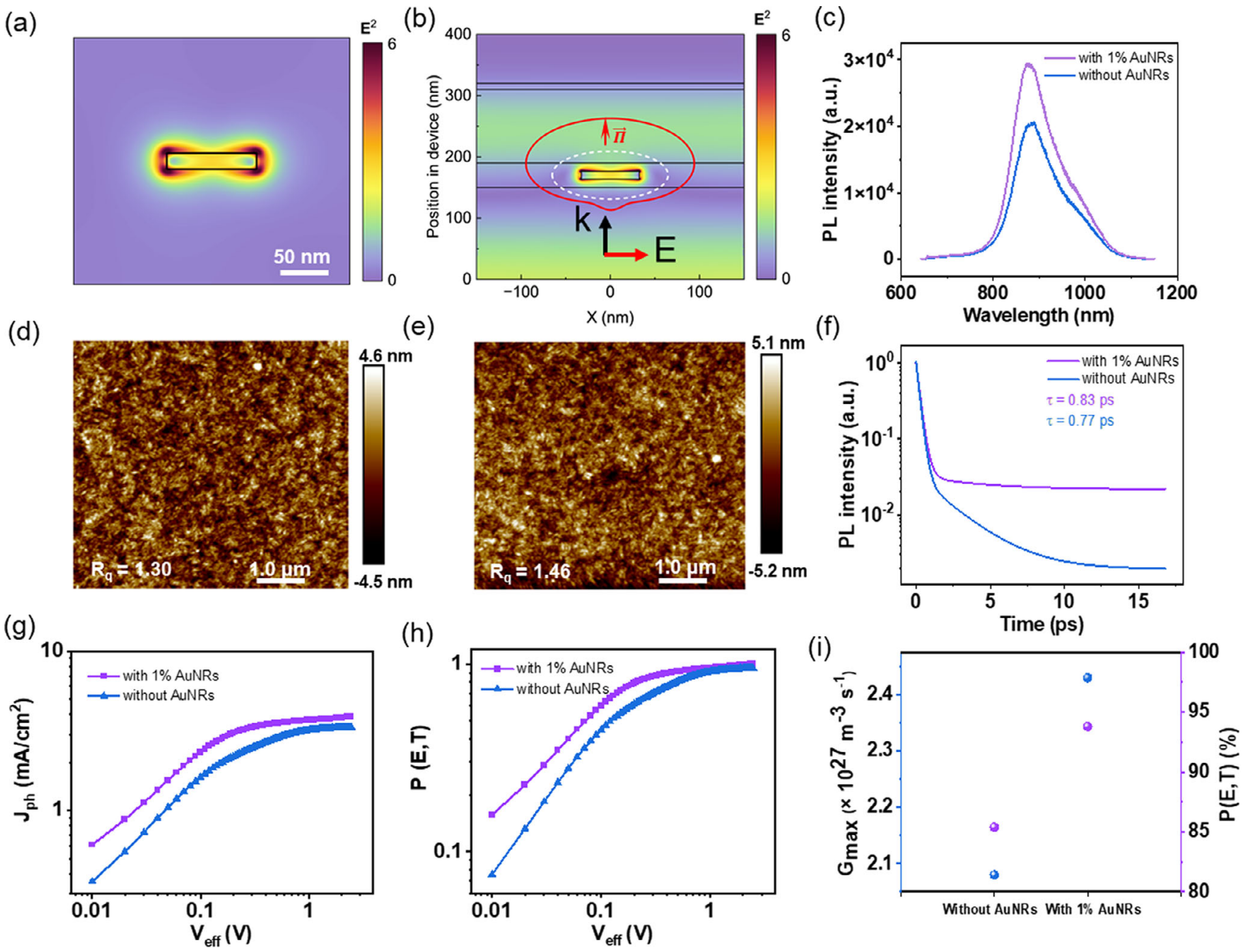

FIGURE 4 | (a) Distribution of the electric field intensity of AuNRs under excitation of 820 nm light and (b) their corresponding electric field distribution within the OPSs. The scattering diagrams, plotted in red around AuNRs, represent the Poynting vector $\vec{\Pi}$ along the white-dashed ellipsoids. AFM images measured for the PM6:L8-BO blend layers coated on (c) a pristine PEDOT:PSS HBL and (d) the hybrid PEDOT:PSS:AuNRs HBL. (e) PL spectra of ITO/PEDOT:PSS/L8-BO and ITO/PEDOT:PSS:AuNRs/L8-BO thin films. (f) TRPL decay curves of ITO/PEDOT:PSS/PM6:L8-BO and ITO/PEDOT:PSS:AuNRs/PM6:L8-BO thin films deposited on quartz substrates. (g) J_{ph}–V_{eff} curves. (h) $P(E,T)$–V_{eff} curves. (i) The values of $G_{\max}$ and $P(E,T)$ obtained for OPSs fabricated without and with AuNRs, respectively.

are well embedded within the PEDOT:PSS layer and exert minimal impact on the film-forming quality of the overlying PM6:L8-BO layer. To further investigate the influence of LSPR on exciton dynamics, steady-state photoluminescence (PL) measurements were performed on ITO/PEDOT:PSS:AuNRs/L8-BO and ITO/PEDOT:PSS/L8-BO films. As shown in Figure 4e, under 800 nm excitation, the PL intensity of the active layer incorporating AuNRs exhibits a 43.91% enhancement compared to the control film. Moreover, it also indicates that exciton quenching at the interface between the PEDOT:PSS:AuNRs EBL and the active layer is effectively suppressed, which is beneficial for improving the device's EPSC. This enhancement is primarily attributed to the LSPR effect of the AuNRs, which strengthens the NIR light absorption capability of L8-BO, as shown in Figure 4b. To gain further insight into the carrier dynamics, time-resolved photoluminescence (TRPL) measurements were performed on OPS incorporating AuNRs and on a control device employing pristine PEDOT:PSS as the EBL, as shown in Figure 4f. The exciton lifetime was determined by fitting the PL decay process using the following biexponential function [76]:

$$\tau = A_1 e^{-x/\tau_1} + A_2 e^{-x/\tau_2} \tag{5}$$

Here, A_1 and A_2 represent the amplitudes of the first and second decay components, while τ_1 and τ_2 denote the corresponding exponential decay constants. The AuNRs-doped device exhibited a reduced exciton lifetime of 0.77 ps compared to 0.83 ps for the control device. This decrease is indicative of more efficient exciton dissociation, likely facilitated by the intense localized electric field near the AuNRs. These results are in good agreement with both experimental data and FEM simulations. Specifically, the presence of AuNRs within the EBL was shown to generate a strong LSPR effect, producing an amplified near-field that penetrates the active layer (Figure 4b). This configuration avoids the exciton quenching typically associated with blending nanometallic structures directly into the active layer, thus preserving charge generation efficiency while leveraging plasmonic enhancement [77].

26924560, 2026, 3, Downloaded from https://onlinelibrary.wiley.com/doi/10.1002/agt2.70319 by HONG KONG POLYTECHNIC UNIVERSITY HU NG HOM, Wiley Online Library on [10/04/2026]. See the Terms and Conditions (https://onlinelibrary.wiley.com/terms-and-conditions) on Wiley Online Library for rules of use; OA articles are governed by the applicable Creative Commons License

Beyond the optical absorption enhancement, the overall improvement in photovoltaic performance can also be attributed to factors such as exciton dissociation, charge transport, and carrier collection efficiency [78]. To evaluate the influence of AuNRs incorporated into the EBL on charge extraction, the photocurrent density (J_{ph}) versus effective voltage (V_{eff}) characteristics of OPSs were investigated, as shown in Figure 4g [79]. Here, J_{ph} is defined as $J_{\mathrm{ph}} = J_{\mathrm{L}} - J_{\mathrm{D}}$, where J_{L} represents the current density under 0.51 mW cm^{-2}, and J_{D} denotes the dark current density. The effective voltage is given by $V_{\mathrm{eff}} = V_0 - V_{\mathrm{a}}$, with V_0 as the built-in potential and V_{a} the applied bias. At low V_{eff}, bimolecular recombination limits carrier collection, resulting in incomplete extraction of photogenerated carriers. As V_{eff} increases (>0.6 V), nearly all photogenerated carriers are effectively extracted, leading to a saturated photocurrent density (J_{sat}). Assuming that all the photogenerated excitons are dissociated into free charge carriers and collected without the recombination loss under the high effective voltage, then the maximum exciton generation rate (G_{max}) could be determined by the equation $J_{\mathrm{sat}} = qG_{\mathrm{max}}L$, where q is the elementary charge and L is the BHJ thickness. The values of G_{max} calculated for the control device and AuNRs-modified device are 2.08×10^{27} and 2.43×10^{27} m^{-3} s^{-1}, respectively. The higher G_{max} indicates that the charge generation efficiency of the AuNRs-modified device is greater than that of the control device, leading to a higher output current at 808 nm. Both the control device and the AuNRs-modified device exhibit saturation at a similar V_{eff}, yet the latter achieves a higher J_{ph}, indicating improved exciton dissociation efficiency $P(E,T)$. As presented in Figure 4h,i, under low bias conditions ($V_{\mathrm{eff}} < 0.3$ V), the $P(E,T)$ for the AuNRs-based OPS reaches 93.8%, which is significantly higher than the 85.4% observed in the control device. This enhancement confirms that the hybrid AuNRs–PEDOT:PSS EBL facilitates more efficient exciton separation in the active layer.

The retina of the human eye is highly efficient in processing image information and can simultaneously perceive and process. Human visual memory is usually defined as a process of "learning–forgetting–relearning" [80]. The intensity of external stimuli is directly related to memory strength. By increasing the intensity of stimuli, STM can be transformed into LTM [81]. To explore the performance of the doped BHJ-OPS device prepared in this work in terms of image recognition and memory, herein, we conducted simulation training of the pattern recognition and memory process using a 5 × 5 array device, where the learning and forgetting processes of the array device can be associated with the conductance states during and after stimulation, respectively. Each image pixel is represented by one BHJ-OPS device, and the real-time current of each device is displayed in the form of a heat map. As shown in Figure 5, during the training process, we used 808 nm light pulses as stimuli and encoded and memorized the three characters "H," "E," and "F" in sequence with one, four, and seven pulses (pulse width of 1 s), respectively. As shown in Figure 5a, the array displays the character "H" after being stimulated by one light pulse, simulating the neural memory process. However, within the following 20 s, as the light pulse was removed, the current value of the device gradually decreased, and the "H" character gradually became very blurred. This process is very similar to the "forgetting process" of human vision. This also indicates that the device's memory of a single optical pulse stimulus is not "deep" and is insufficient to retain image information. The "E" letter memorized by applying four consecutive light pulses, as shown in Figure 5b, can still retain relatively clear image information after a 20 s of forgetting process, while the "F" letter memorized by applying seven consecutive light pulses has a much slower forgetting process. A complete and clear image contour can still be presented after a 20 s of forgetting process (Figure 5c). This result is consistent with the previous device synaptic plasticity test experiments, indicating that by increasing the number of pulses, the device can achieve the transformation from STM to LTM, thereby effectively simulating the characteristics of human visual memory.

To investigate the capabilities of AuNRs-doped BHJ-OPS device as an artificial vision system in the realm of image recognition, we further designed and fabricated a 26 × 26 BHJ-OPS device array, as illustrated in Figure 6a. Owing to the excellent adaptability of the doped BHJ-OPS device, we initially preprocessed and denoised blurred handwritten digit images such as "7" and "2" from the MNIST database under both weak light and strong light conditions. The resulting images preserved the essential information of the original images (Figure 6b–e). Subsequently, we simulated the recognition process of these denoised handwritten digit images using a CNN algorithm facilitated by the doped BHJ-OPS device. As depicted in Figure 6f, this CNN architecture comprises two convolutional layers, two pooling layers, and three fully connected layers. The output vector is derived by multiplying the synaptic weight matrix with the input vector followed by transformation through a ReLU activation function. We calculated the neural network weights based on the discrepancies between output values and corresponding label values using gradient descent and backpropagation (BP) algorithms. The constructed 26 × 26 BHJ-OPS device array was utilized as a static visual information processor for unsupervised hue mapping within CNNs to mitigate external interference during recognition tasks. Then, the handwritten digit images that had been preprocessed by the BHJ-OPS device were used from the MNIST database for training and testing purposes. Each training cycle encompassed approximately 60,000 sessions, and each session consisted of randomly ordered training images representing MNIST handwritten digits ranging from 0 to 9 (i.e., each digit underwent roughly 6000 learning sessions). Figure 6g,h illustrates how loss rate variations and recognition accuracy trends evolve over time for both training sets and test sets throughout increasing training periods, respectively. It can be seen clearly that after 100 training cycles, the recognition accuracy of the CNN algorithm based on BHJ-OPS gradually increases and reaches saturation at around 98.57%. Figure 6i shows the confusion matrix results of the CNN model in recognizing images with noise interference after 100 training cycles, indicating that the numbers from "0" to "9" can be well distinguished.

Dynamic gesture recognition plays a crucial role in various application domains, including healthcare, human-computer interaction, and cognitive neuroscience research [82]. To further validate the functionality of the doped BHJ-OPS device as an event camera for dynamic gesture recognition, we developed a CSNN model based on the CNN algorithm. As illustrated in Figure 7a, the CSNN comprises four convolutional layers, two pooling layers, and three fully connected layers. The output pulse sequence is generated through spatiotemporal integration of the synaptic weight matrix with the input event frame

26924560, 2026, 3, Downloaded from https://onlinelibrary.wiley.com/doi/10.1002/agt2.70319 by HONG KONG POLYTECHNIC UNIVERSITY HU NG HOM, Wiley Online Library on [10/04/2026]. See the Terms and Conditions (https://onlinelibrary.wiley.com/terms-and-conditions) on Wiley Online Library for rules of use; OA articles are governed by the applicable Creative Commons License

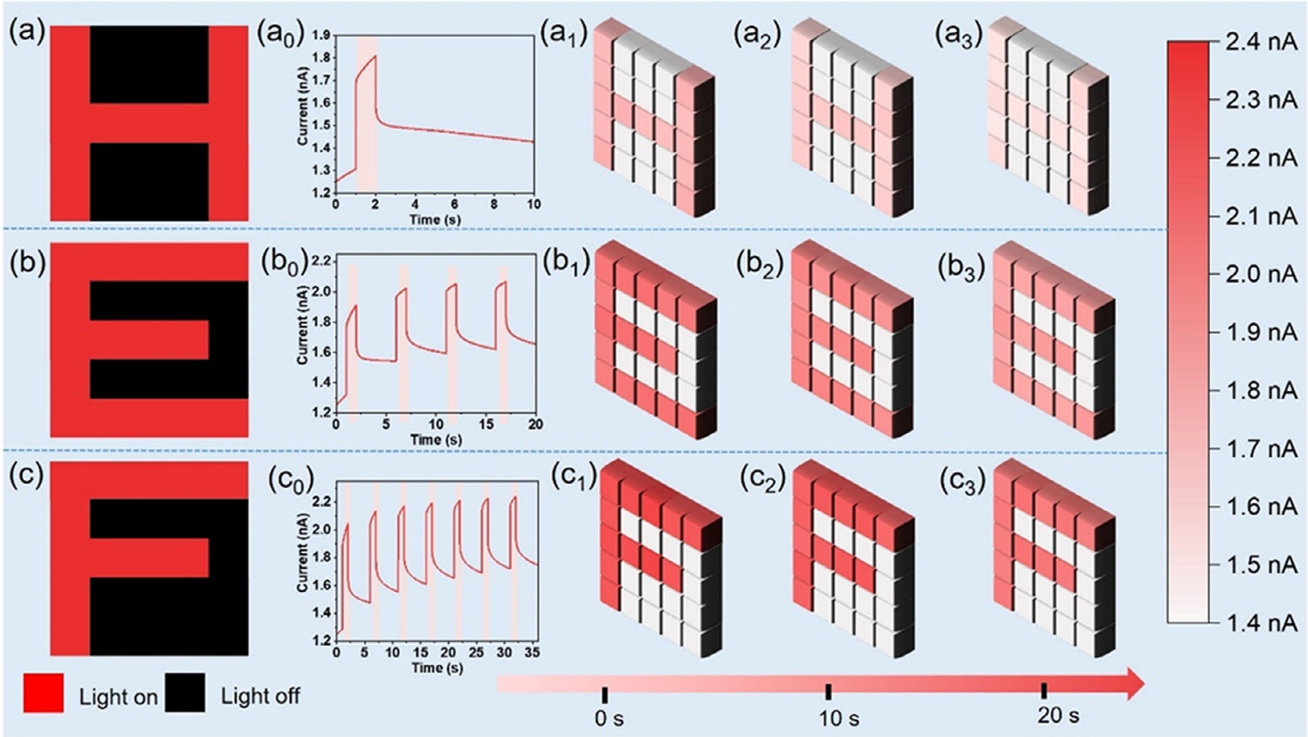

FIGURE 5 | (a–c) are the "H," "E," and "F" shaped letter masks, respectively. (a$_1$–a$_3$) are the image mappings at three time points of 0, 10, and 20 s, respectively, after irradiating the doped BHJ-OPS device with (a$_0$) one pulse of 808 nm light under "H" shaped letter mask. (b$_1$–b$_3$) are the image mappings at three time points of 0, 10, and 20 s, respectively, after irradiating the doped BHJ-OPS device with (b$_0$) four pulses of 808 nm light under "E" shaped letter mask. (c$_1$–c$_3$) are the image mappings at three time points of 0, 10, and 20 s, respectively, after irradiating the doped BHJ-OPS device with (c$_0$) seven pulses of 808 nm light under "F" shaped letter mask.

and subsequently processed using the Leaky Integrate-and-Fire (LIF) neuron model. During training, an alternative gradient method—such as the ATAN function—is employed to approximate the impulse gradient, thereby replacing traditional BP algorithms to address issues related to impulse neuron discreteness. We trained and evaluated the CSNN model utilizing the DVS128Gesture dataset, which contains 1464 samples, representing 11 distinct gestures captured by Dynamic Vision Sensor (DVS) cameras under three different lighting conditions. These gestures are represented as event streams with point clouds that illustrate spatiotemporal variations recorded by DVS technology. The dynamic characteristics inherent in these events enable effective tracking and classification of gestures via neural networks.

In comparison to conventional frame-based cameras, event cameras significantly minimize data redundancy and processing time. The number of linearly programmable conductance states alongside effective conductance states is pivotal for achieving recognition accuracy and efficiency within neuromorphic computing frameworks. Leveraging both a wide range of conductance variation and an approximately linear weight update methodology afforded by the doped BHJ-OPS device allows us to simulate dynamic gesture recognition tasks based on the as-established CSNN model. Figure 7b depicts five distinct human gestures: left-hand waving, arm-clamping rolling, clapping, right arm counterclockwise rotation, and left arm counterclockwise rotation. Figure 7c presents a visualization window for the CSNN model's predictions of five distinct motion gestures, respectively. It is evident that the dynamic characteristics of the events depicted in Figure 7b enable the CSNN model, which utilizes the BHJ-OPS device, to effectively track and classify these gestures. Figure 7d,e illustrates the relationship between the loss rate and recognition accuracy of the CSNN model relative to the number of training sessions. After completing 150 iterations of training, the recognition accuracy achieved by the CSNN model based on the BHJ-OPS device for dynamic gestures reached an impressive 92.01%. Figure 7f displays the confusion matrix corresponding to the recognition results produced by the CSNN model, manifesting that all 11 motion gestures within the DVS128Gesture dataset can be recognized precisely. Consequently, it can be concluded that the CSNN model utilizing doped BHJ-OPS device array exhibits rapid learning capabilities and demonstrates exceptional performance in processing and classifying complex spatial-temporal patterns.

3 | Conclusion

In conclusion, by introducing the LSPR effect of AuNRs, we have successfully developed a high-performance NIR BHJ-OPS with a simple two-terminal structure. The experimental results show that the doped AuNRs significantly enhance the NIR absorption ability of the device, increase the photo-generated exciton yield by 17%, and improve the exciton dissociation efficiency by 8.4%. At the same time, it effectively optimized the synaptic plasticity performance such as PPF index (114.6%), SNDP, STDP, and SIDP. The device verified its potential in image recognition,

26924560, 2026, 3, Downloaded from https://onlinelibrary.wiley.com/doi/10.1002/agt2.70319 by HONG KONG POLYTECHNIC UNIVERSITY HU NG HOM, Wiley Online Library on [10/04/2026]. See the Terms and Conditions (https://onlinelibrary.wiley.com/terms-and-conditions) on Wiley Online Library for rules of use; OA articles are governed by the applicable Creative Commons License

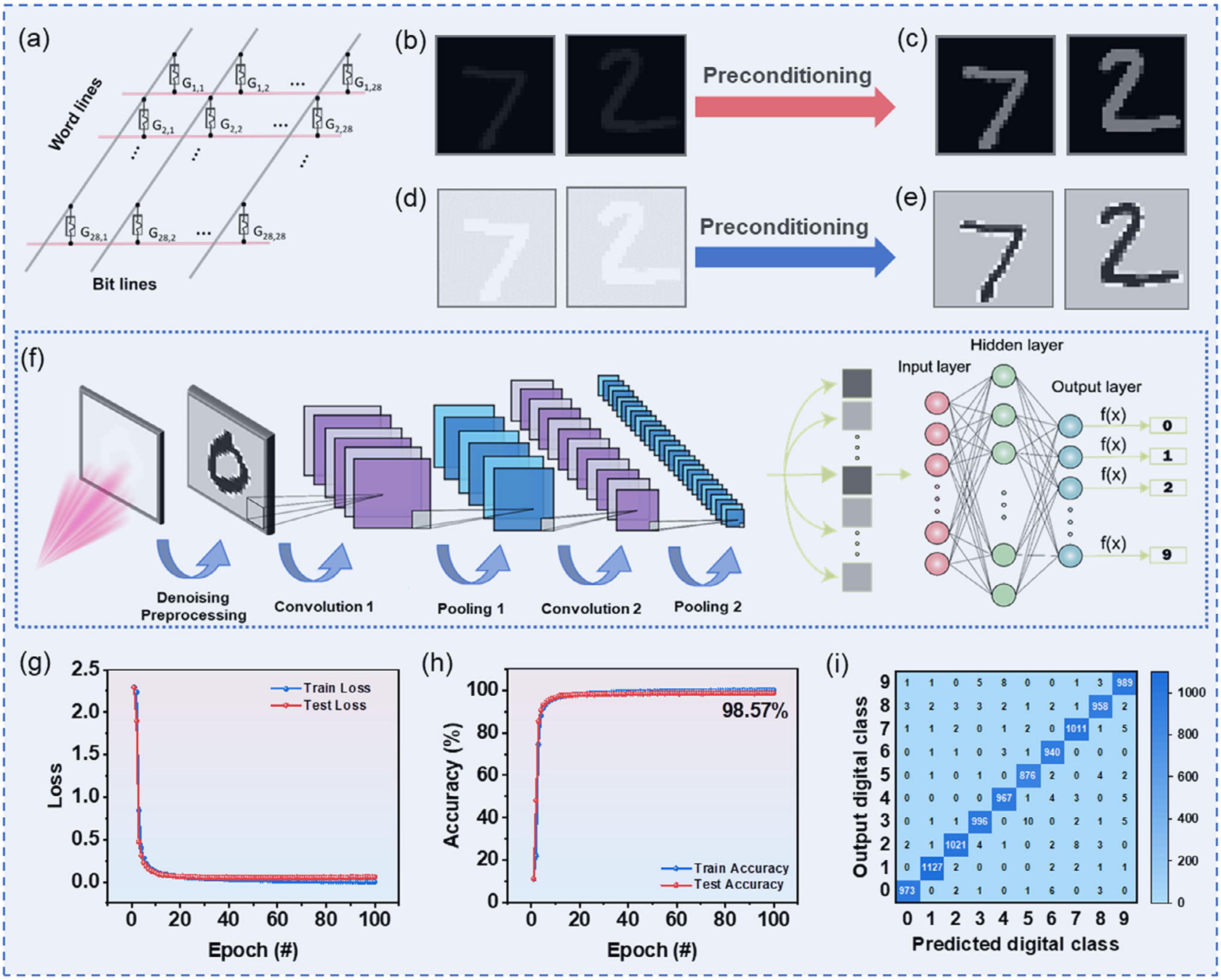

FIGURE 6 | (a) Architecture of a BHJ-OPS array with word lines and bit lines. Handwritten digit images under dim light conditions (b) before and (c) after preprocessing by the BHJ-OPS array. Handwritten digit images under strong light interference conditions (d) before and (e) after preprocessing by the BHJ-OPS array. (f) Schematic diagram of the CNN. (g) Loss rate variation curve and (h) recognition accuracy variation curve of the CNN over 100 training epochs. (i) Confusion matrix results of image recognition tasks under noisy interference.

memory, and dynamic information processing by simulating the "learning–forgetting–relearning" process of human vision. The doped BHJ-OPS-based CNN model has an accuracy rate of up to 98.57% in recognizing MINST handwritten digits under strong light interference and dim light conditions, demonstrating its excellent adaptability. Finally, the CSNN model based on doped BHJ-OPS that we built achieved a recognition accuracy of 92.01% in the dynamic gesture recognition task after 150 iterations of training, indicating its high efficiency in neuromorphic computing. Compared with traditional NIR synaptic devices, the high-performance AuNRs-doped BHJ-OPS device reported in this work is achieved through a simple solution processing technology, with no need of complex and expensive organic semiconducting material design and synthesis. Moreover, the high chemical stability (not prone to oxidation) and tunable LSPR characteristics of AuNRs provide a guarantee for the long-term stability and spectral adaptability of the device. Consequently, this work expands the application scenarios of organic semiconductors in brain-like devices, providing a new paradigm for the development of low-cost and highly compatible NIR neuromorphic devices, and is expected to promote the development of fields such as flexible artificial night vision systems, intelligent driving visual perception, and portable medical imaging.

4 | Experimental Section

4.1 | Synthesis of AuNRs

To prepare the gold seed solution, 10 mL of CTAB (0.1 M) was mixed with 0.25 mL of $HAuCl_4$ (0.01 M), followed by the rapid addition of 0.60 mL $NaBH_4$ (0.01 M) under vigorous stirring for 2 min. The resulting brownish solution was aged at room temperature for at least 2 h before use. For the growth solution, 1.0 mL of $HAuCl_4$ (0.01 M) and 0.20 mL of $AgNO_3$ (0.01 M) were added to 20 mL of CTAB (0.1 M), followed by 0.4 mL of HCl (1.0 M) to adjust the pH to 1–2. Subsequently, 0.16 mL of ascorbic acid (0.1 M) was added with gentle stirring for 30 s. Then, 40 µL of the seed solution was injected, and the mixture was gently stirred for 10 s and left undisturbed at room temperature for 12 h. The color

26924560, 2026, 3, Downloaded from https://onlinelibrary.wiley.com/doi/10.1002/agt2.70319 by HONG KONG POLYTECHNIC UNIVERSITY HU NG HOM, Wiley Online Library on [10/04/2026]. See the Terms and Conditions (https://onlinelibrary.wiley.com/terms-and-conditions) on Wiley Online Library for rules of use; OA articles are governed by the applicable Creative Commons License

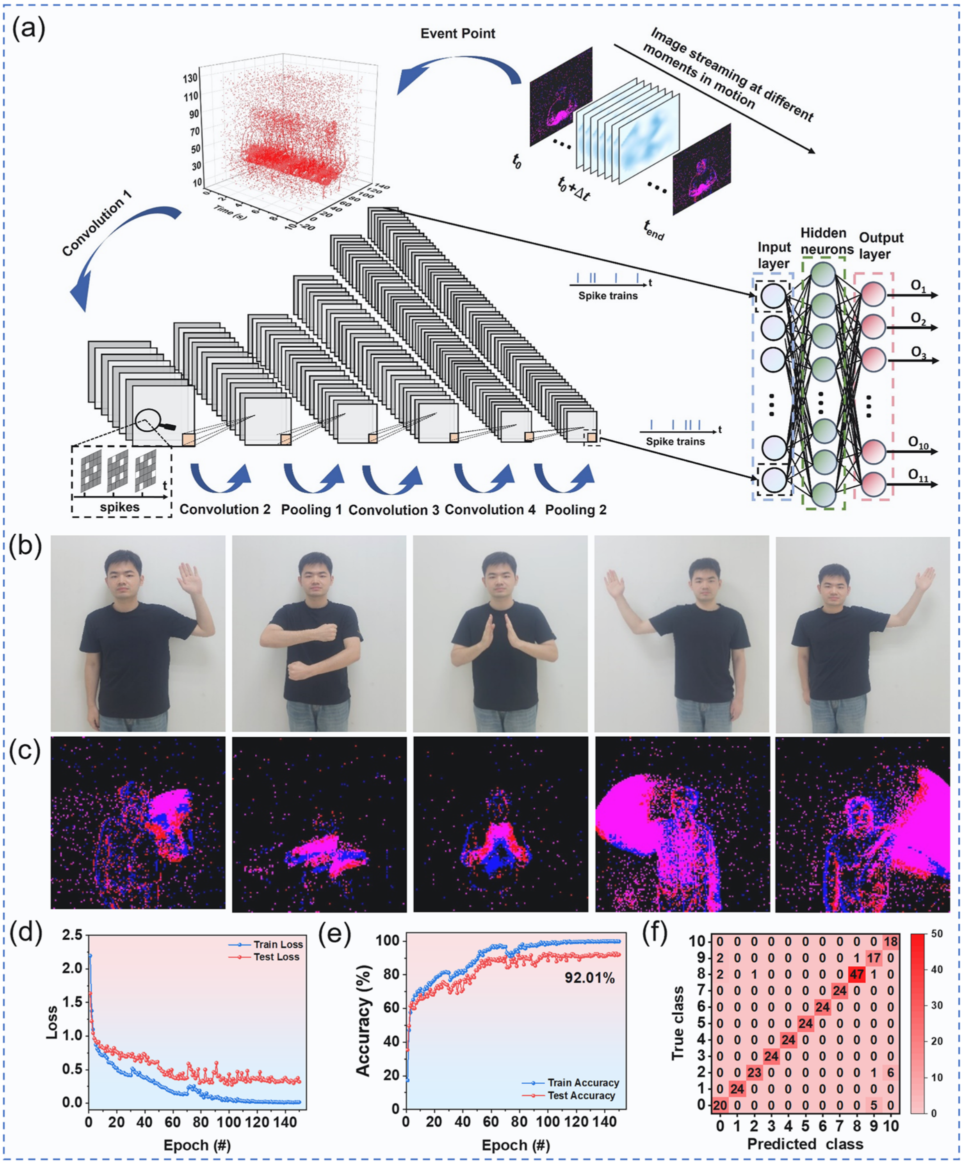

FIGURE 7 | (a) Schematic diagram of the CSNN. (b) 24-bit RGB video frames of the gestures used in this experiment. From left to right, the gestures are left-hand waving, arm-clamping rolling, clapping, right arm counterclockwise rotation, and left arm counterclockwise rotation. (c) "Frames" of the DVS, generated by superimposing pulses within the window starting from each RGB video frame. (d) Loss rate variation curve and (e) recognition accuracy variation curve of the CSNN over 150 training epochs. (f) Confusion matrix results of the CSNN model for dynamic gesture recognition tasks after 150 training epochs.

change to dark red indicated the formation of gold nanorods. The product was then purified by centrifugation at 8000 rpm for 30 min. The supernatant was discarded, and the precipitate was redispersed in deionized water. This washing step was repeated three times to give rise to the final AuNRs solution for use in next device fabrication.

4.2 | Materials Preparation

PEDOT:PSS (Clevios P VP AI 4083) was obtained from Xi'an Polymer Light Technology Corp. The donor material PM6 and the non-fullerene acceptor L8-BO were sourced from Organtec Ltd. 1,8-Diiodooctane (DIO) and chloroform (CF) were supplied by Sigma-Aldrich, while PFN-Br was provided by Luminescence Technology Corp. All chemicals were used as received, without any additional purification.

4.3 | Device Fabrication

ITO/glass substrates with a sheet resistance of 15 Ω sq^{-1} were sequentially cleaned via ultrasonication in detergent, acetone, isopropanol, and deionized water, each for 30 min. Following this wet cleaning process, the substrates underwent ozone treatment for 15 min. A layer of pristine PEDOT:PSS or PEDOT:PSS:AgNRs (1 wt% AuNRs doped into PEDOT:PSS) was then spin-coated onto the cleaned substrates at 3000 rpm for 60 s, followed by thermal annealing in air at 130°C for 20 min, resulting in a 40 nm-thick EBL. Subsequently, a blend solution of PM6 and L8-BO

26924560, 2026, 3, Downloaded from https://onlinelibrary.wiley.com/doi/10.1002/agt2.70319 by HONG KONG POLYTECHNIC UNIVERSITY HU NG HOM, Wiley Online Library on [10/04/2026]. See the Terms and Conditions (https://onlinelibrary.wiley.com/terms-and-conditions) on Wiley Online Library for rules of use; OA articles are governed by the applicable Creative Commons License

(16 mg mL^{-1}, weight ratio 1:1.2) in CF containing 0.5% DIO was deposited onto the EBL by spin-coating at 3000 rpm for 30 s. The film was then thermally annealed at 110°C for 20 min inside a nitrogen-filled glovebox to form an active layer with a thickness of approximately 120 nm. A 5 nm interlayer of PFN-Br was spin-coated as the HBL, followed by deposition of a 20 nm silver top electrode via thermal evaporation. The fabricated BHJ-OPS arrays featured active areas defined by the overlap of the ITO and top electrode: 0.2×0.2 cm^2 for the 5×5 array and 20×20 cm^2 for the 26×26 array.

4.4 | Characterization

SEM analysis was conducted by utilizing a QUANTA FEG 450 field emission microscope. Surface morphologies of the films were characterized by AFM (Nanonavi SPA-400 SPM). Charge carrier mobility was measured using a Hall measurement system (Chaoruirenda Technology, CR-cryo4) equipped with a Source meter (Keithley 2450). The details of the measurement can be found in Figures S10 and S11 and Tables S1 and S2. The absorption spectra of the functional layers were recorded using a UV-vis spectrophotometer (HITACHI Ue3900H). TRPL spectra were obtained with a fluorescence spectrometer (FLSP 920). All electrical assessments were conducted with a PDA FS-Pro system, utilizing a probe station for precise device contact. Monochromatic illumination was achieved using a 150 W xenon lamp in combination with appropriate monochromators, while vis-NIR light was supplied by LEDs.

4.5 | Weight Update Method

The method for updating synaptic weights relies on the nonlinearity (NL) extracted from the experimentally obtained LTP and LTD characteristics. The NL values corresponding to potentiation and depression were obtained by fitting the LTP/LTD curves, using the following equations:

$$G_{n+1} = G_n + \triangle G_p = G_n + \alpha_p e^{-\beta_p \frac{G_n - G_{\min}}{G_{\max} - G_{\min}}} \tag{6}$$

$$G_{n+1} = G_n + \triangle G_d = G_n + \alpha_d e^{-\beta_d \frac{G_{\max} - G_n}{G_{\max} - G_{\min}}} \tag{7}$$

Here, G_n denotes the synaptic conductance at the nth stimulation cycle, while G_{n+1} refers to the conductance after applying the weight update. The conductance variation is represented by ΔG. The terms α and β correspond to the update step size and the degree of NL, respectively, as defined by Equations (6) and (7). Synaptic weight modulation was carried out using conductance values obtained from both LTP and LTD processes under different NL conditions.

4.6 | Theoretical simulation

Optical field distributions within different thin film structures were simulated using COMSOL Multiphysics. The device architecture was modeled as glass (semi-infinite)/ITO (150 nm)/HBL (40 nm, either PEDOT:PSS or AuNRs:PEDOT:PSS)/PM6:L8-BO (120 nm)/PFN-Br (5 nm)/Ag (100 nm). The optical constants for the PM6:L8-BO blend, pristine PEDOT:PSS, and AuNBPs:PEDOT:PSS films were measured using an RC2-XI ellipsometer (J.A. Woollam). In the model, AuNRs were positioned at the center of the PEDOT:PSS matrix, with their geometric features aligned with experimental observations. The simulation employs normally incident light from the semi-infinite glass side, linearly polarized along the *X*-axis. The electric field distribution and light scattering patterns in the active layer were computed across the NIR spectrum.

Acknowledgments

We thank the support from National Natural Science Foundation of China (Grant Numbers: 62174116, 61774109, and 92477120).

Conflicts of Interest

The authors declare no conflicts of interest.

References

1. W.-S. Khwa, T. H. Wen, H. H. Hsu, et al., “A Mixed-Precision Memristor and SRAM Compute-in-Memory AI Processor,” *Nature* 639 (2025): 617–623.

2. A. Mehonic and A. J. Kenyon, “Brain-Inspired Computing Needs a Master Plan,” *Nature* 604 (2022): 255–260.

3. D. Kumar, H. Li, D. D. Kumbhar, et al., “Highly Efficient Back-End-of-Line Compatible Flexible Si-Based Optical Memristive Crossbar Array for Edge Neuromorphic Physiological Signal Processing and Bionic Machine Vision,” *Nano-Micro Letters* 16 (2024): 238.

4. M. A. Zidan, J. P. Strachan, and W. D. Lu, “The Future of Electronics Based on Memristive Systems,” *Nature Electronics* 1 (2018): 22–29.

5. A. M. Syed, D. D. Kumbhar, H. Li, et al., “A Multimodal Humidity Adaptive Optical Neuron Based on a MoWS$_2$/VO$_X$ Heterojunction for Vision and Respiratory Functions,” *Advanced Materials* 37 (2025): 2417793.

6. H. Wang, B. Sun, S. S. Ge, et al., “On Non-Von Neumann Flexible Neuromorphic Vision Sensors,” *npj Flexible Electronics* 8 (2024): 28.

7. M. V. Wilkes, “The Memory Wall and the CMOS End-Point,” *ACM SIGARCH Computer Architecture News* 23 (1995): 4–6.

8. H. Tanaka, M. Akai-Kasaya, A. TermehYousefi, et al., “A Molecular Neuromorphic Network Device Consisting of Single-Walled Carbon Nanotubes Complexed With Polyoxometalate,” *Nature Communications* 9 (2018): 2693.

9. J. J. Yang, J. Grollier, R. S. Williams, et al., “Neuromorphic Engineering: From Materials to Device Application,” *Advanced Materials* 35 (2023): 2305078.

10. K. Liu, T. Zhang, B. Dang, et al., “An Optoelectronic Synapse Based on *α*-In2Se3 With Controllable Temporal Dynamics for Multimode and Multiscale Reservoir Computing,” *Nature Electronics* 5 (2022): 761–773.

11. Y. Lee and T. W. Lee, “Organic Synapses for Neuromorphic Electronics: From Brain-Inspired Computing to Sensorimotor Nervetronics,” *Accounts of Chemical Research* 52 (2019): 964–974.

12. W. Zhang, B. Gao, J. Tang, et al., “Neuro-Inspired Computing Chips,” *Nature Electronics* 3 (2020): 371–382.

13. L. Chen, R. Li, S. Yuan, et al., “Fiber-Shaped Artificial Optoelectronic Synapses for Wearable Visual-Memory Systems,” *Matter* 6 (2023): 925–939.

14. Q. Wan, X. Y. Jiang, A. M. Negroiu, et al., “Protein Kinase C Acts as a Molecular Detector of Firing Patterns to Mediate Sensory Gating in Aplysia,” *Nature Neuroscience* 15 (2012): 1144–1152.

15. G. Wang, R. Wang, W. Kong, et al., “Simulation of Retinal Ganglion Cell Response Using Fast Independent Component Analysis,” *Cognitive Neurodynamics* 12 (2018): 615–624.

26924560, 2026, 3, Downloaded from https://onlinelibrary.wiley.com/doi/10.1002/agt2.70319 by HONG KONG POLYTECHNIC UNIVERSITY HU NG HOM, Wiley Online Library on [10/04/2026]. See the Terms and Conditions (https://onlinelibrary.wiley.com/terms-and-conditions) on Wiley Online Library for rules of use; OA articles are governed by the applicable Creative Commons License

16. P. Yao, H. Wu, B. Gao, et al., “Face Classification Using Electronic Synapses,” *Nature Communications* 8 (2017): 15199.

17. P. M. Sheridan, F. Cai, C. Du, et al., “Sparse Coding With Memristor Networks,” *Nature Nanotechnology* 12 (2017): 784–789.

18. C. Li, G. Chen, Y. Zhang, et al., “Advanced Fluorescence Imaging Technology in the Near-Infrared-II Window for Biomedical Applications,” *Journal of the American Chemical Society* 142 (2020): 14789–14804.

19. Y. He, H. Liao, S. Lyu, et al., “Coupling Molecular Rigidity and Flexibility on Fused Backbones for NIR-II Photothermal Conversion,” *Chemical Science* 12 (2021): 5177–5184.

20. C. Sun, B. Li, M. Zhao, et al., “J-aggregates of Cyanine Dye for NIR-II In Vivo Dynamic Vascular Imaging Beyond 1500 Nm,” *Journal of the American Chemical Society* 141 (2019): 19221–19225.

21. B. Zhou, L. Yan, J. Huang, et al., “NIR II-Responsive Photon Upconversion Through Energy Migration in an Ytterbium Sublattice,” *Nature Photonics* 14 (2020): 760–766.

22. F. Zhou, Z. Zhou, J. Chen, et al., “Optoelectronic Resistive Random Access Memory for Neuromorphic Vision Sensors,” *Nature Nanotechnology* 14 (2019): 776–782.

23. H. L. Park, H. Kim, D. Lim, et al., “Retina-Inspired Carbon Nitride-Based Photonic Synapses for Selective Detection of UV Light,” *Advanced Materials* 32 (2020): 1906899.

24. L. Hu, J. Yang, J. Wang, et al., “All-Optically Controlled Memristor for Optoelectronic Neuromorphic Computing,” *Advanced Functional Materials* 31 (2021): 2005582.

25. Y. X. Hou, Y. Li, Z.-C. Zhang, et al., “Large-Scale and Flexible Optical Synapses for Neuromorphic Computing and Integrated Visible Information Sensing Memory Processing,” *ACS Nano* 15 (2020): 1497–1508.

26. Y. Wang, Y. Zhu, Y. Li, et al., “Dual-Modal Optoelectronic Synaptic Devices With Versatile Synaptic Plasticity,” *Advanced Functional Materials* 32 (2022): 2107973.

27. H. Shao, Y. Li, W. Yang, et al., “A Reconfigurable Optoelectronic Synaptic Transistor With Stable Zr-$CsPbI_3$ Nanocrystals for Visuomorphic Computing,” *Advanced Materials* 35 (2023): 2208497.

28. C. Liu, C. Gao, W. Huang, et al., “Bipolar Synaptic Organic/Inorganic Heterojunction Transistor With Complementary Light Modulation and Low Power Consumption for Energy-Efficient Artificial Vision Systems,” *Science China Materials* 67 (2024): 1500–1508.

29. Z. He, H. Duan, J. Zeng, et al., “Perovskite Retinomorphic Image Sensor for Embodied Intelligent Vision,” *Science Advances* 11 (2025): eads2834.

30. S. Lan, J. Zhong, J. Chen, et al., “An Optoelectronic Synaptic Transistor With Efficient Dual Modulation by Light Illumination,” *Journal of Materials Chemistry C* 9 (2021): 3412–3420.

31. M. K. Rajbhar, D. Kumar, H. Li, et al., “Fully Photonic Controlled Flexible Synapse for Bionic Machine Vision and Reconfigurable Logic Applications,” *Materials Science and Engineering: R: Reports* 167 (2026): 101088.

32. K. Chong, X. Xu, H. Meng, et al., “Realizing 19.05% Efficiency Polymer Solar Cells by Progressively Improving Charge Extraction and Suppressing Charge Recombination,” *Advanced Materials* 34 (2022): 2109516.

33. J. Lee, S. J. Ko, H. Lee, et al., “Side-Chain Engineering of Nonfullerene Acceptors for Near-Infrared Organic Photodetectors and Photovoltaics,” *ACS Energy Letters* 4 (2019): 1401–1409.

34. T. Liu, Q. Lin, Y. Ma, et al., “Multifunctional Organic Vertical Photodiodes for Photo-Detection and Photo-Synapse Enabled by Modulation of the Interface Energy Barrier,” *Advanced Optical Materials* 10 (2022): 2201104.

35. Y. Wei, Y. Liu, Q. Lin, et al., “Organic Optoelectronic Synapses for Sound Perception,” *Nano-Micro Letters* 15 (2023): 133.

36. L. Jiang, L. Yang, Y. Yuan, et al., “Flexible Optoelectronic Synapses Based on Conjugated Polymer Blends for Ultra Broadband Spectrum Light Perception,” *ACS Materials Letters* 6 (2024): 1606–1615.

37. H. Shao, Y. Ji, R. Wang, et al., “Optically Enhanced Organic Phototransistors for Adaptive Image Processing Under Complex Light Conditions,” *Nano Energy* 130 (2024): 110133.

38. H. Lian, S. Wang, Z. Qin, et al., “Transparent and Flexible Organic Bulk Heterojunction Photonic Synapse for Neuromorphic Computing and Reflex Arc Behavior,” *Device* 3 (2025): 100749.

39. W. Chen, Z. Zhang, and G. Liu, “Retinomorphic Optoelectronic Devices for Intelligent Machine Vision,” *iScience* 25 (2022): 103729.

40. M. T. Vijjapu, M. E. Fouda, A. Agambayev, et al., “A Flexible Capacitive Photoreceptor for the Biomimetic Retina,” *Light: Science & Applications* 11 (2022): 3.

41. T. Guo, B. Zhang, X. Wang, et al., “Broadband Optoelectronic Synapse Enables Compact Monolithic Neuromorphic Machine Vision for Information Processing,” *Advanced Functional Materials* 33 (2023): 2303879.

42. D. Kumar, H. Li, U. K. Das, et al., “Flexible Solution-Processable Black-Phosphorus-Based Optoelectronic Memristive Synapses for Neuromorphic Computing and Artificial Visual Perception Applications,” *Advanced Materials* 35 (2023): 2300446.

43. X. Duan, Z. Cao, K. Gao, et al., “Memristor-Based Neuromorphic Chips,” *Advanced Materials* 36 (2024): 2310704.

44. L. Zhang, N. Ding, L. Lou, et al., “Localized Surface Plasmon Resonance Enhanced Photocatalytic Hydrogen Evolution via Pt@Au NRs/C3N4 Nanotubes Under Visible-Light Irradiation,” *Advanced Functional Materials* 29 (2019): 1806774.

45. Y. Wu, Y. Gao, X. Zhuang, et al., “Highly Efficient Near-Infrared Hybrid Perovskite Solar Cells by Integrating With a Novel Organic Bulk-Heterojunction,” *Nano Energy* 77 (2020): 105181.

46. H. Lian, Z. Dou, Z. Qin, et al., “A Polychromatic Neuromorphic Visual System Inspired by Biomimetics for Miniature Insect Robots,” *Advanced Materials* 37 (2025): 2416649.

47. Y. Lin, T. Zeng, H. Xu, et al., “Transferable and Flexible Artificial Memristive Synapse Based on WO_x Schottky Junction on Arbitrary Substrates,” *Advanced Electronic Materials* 4 (2018): 1800373.

48. S. Gao, G. Liu, H. Yang, et al., “An Oxide Schottky Junction Artificial Optoelectronic Synapse,” *ACS Nano* 13 (2019): 2634–2642.

49. C. Gao, D. Liu, C. Xu, et al., “Feedforward Photoadaptive Organic Neuromorphic Transistor With Mixed-Weight Plasticity for Augmenting Perception,” *Advanced Functional Materials* 34 (2024): 2313217.

50. H. Shao, Y. Li, J. Chen, et al., “Mimicking Evasive Behavior in Wavelength-Dependent Reconfigurable Phototransistors With Ultralow Power Consumption,” *SmartMat* 5 (2024): e1230.

51. B. Yang, Y. Lu, D. Jiang, et al., “Bioinspired Multifunctional Organic Transistors Based on Natural Chlorophyll/Organic Semiconductors,” *Advanced Materials* 32 (2020): 2001227.

52. Y. Pan, C. Wu, G. Bu, et al., “All-in-One Neuromorphic Light-Emitting Memristor for Infrared Image Visualization and Recognition,” *Advanced Functional Materials* 35 (2025): 2505174.

53. Y. Hu, H. Yang, J. Huang, et al., “Flexible Optical Synapses Based on In_2Se_3/MoS_2 Heterojunctions for Artificial Vision Systems in the Near-Infrared Range,” *ACS Applied Materials & Interfaces* 14 (2022): 55839–55849.

54. C. Jo, J. Kim, J. Y. Kwak, et al., “Retina-Inspired Color-Cognitive Learning via Chromatically Controllable Mixed Quantum Dot Synaptic Transistor Arrays,” *Advanced Materials* 34 (2022): 2108979.

55. Y. Chen, Y. Huang, J. Zeng, et al., “Energy-Efficient ReS_2-Based Optoelectronic Synapse for 3D Object Reconstruction and Recognition,” *ACS Applied Materials & Interfaces* 15 (2023): 58631–58642.

26924560, 2026, 3, Downloaded from https://onlinelibrary.wiley.com/doi/10.1002/agt2.70319 by HONG KONG POLYTECHNIC UNIVERSITY HU NG HOM, Wiley Online Library on [10/04/2026]. See the Terms and Conditions (https://onlinelibrary.wiley.com/terms-and-conditions) on Wiley Online Library for rules of use; OA articles are governed by the applicable Creative Commons License

56. Y. Wang, J. Yang, Z. Wang, et al., “Near-Infrared Annihilation of Conductive Filaments in Quasiplane $MoSe_2/Bi_2Se_3$ Nanosheets for Mimicking Heterosynaptic Plasticity,” *Small* 15 (2019): 1805431.

57. R. Yang, Y. Wang, S. Li, et al., “All-Optically Controlled Artificial Synapse Based on Full Oxides for Low-Power Visible Neural Network Computing,” *Advanced Functional Materials* 34 (2024): 2312444.

58. X. Yang, Z. Xiong, Y. Chen, et al., “A Self-Powered Artificial Retina Perception System for Image Preprocessing Based on Photovoltaic Devices and Memristive Arrays,” *Nano Energy* 78 (2020): 105246.

59. R. Shen, Y. Jiang, Z. Li, et al., “Near-Infrared Artificial Optical Synapse Based on the P (VDF-TrFE)-Coated InAs Nanowire Field-Effect Transistor,” *Materials* 15 (2022): 8247.

60. Y. Sun, L. Qian, D. Xie, et al., “Photoelectric Synaptic Plasticity Realized by 2D Perovskite,” *Advanced Functional Materials* 29 (2019): 1902538.

61. L. Yin, C. Han, Q. Zhang, et al., “Synaptic Silicon-Nanocrystal Phototransistors for Neuromorphic Computing,” *Nano Energy* 63 (2019): 103859.

62. J. Wang, J. Xu, X. Han, et al., “High-Endurance STO:YSZ Optoelectronic Memristors With Vertically Aligned Nanocomposite Structure for Edge Detection,” *Advanced Science* 13 (2026): e13646.

63. Z. Guo, G. Liu, W. Zhang, et al., “In-Sensor Reservoir Computing for Biometric Identification Based on $MoTe_2/BaTiO_3$ Optical Synapses,” *InfoMat* 7 (2025): e70036.

64. R. Li, W. Wang, Y. Li, et al., “Multi-Modulated Optoelectronic Memristor Based on Ga_2O_3/MoS_2 Heterojunction for Bionic Synapses and Artificial Visual System,” *Nano Energy* 111 (2023): 108398.

65. J. Lan, H. Zhou, H. Li, et al., “Infrared Light-Responsive $CuSbS_2$ Optoelectronic Artificial Synapses Enabling High-Accuracy Color Image Recognition and Classification,” *Journal of Chemical Physics* 163 (2025): 214702.

66. B. Bae, M. Park, D. Lee, et al., “Hetero-Integrated InGaAs Photodiode and Oxide Memristor-Based Artificial Optical Nerve for In-Sensor NIR Image Processing,” *Advanced Optical Materials* 11 (2023): 2201905.

67. J. Luo, X. Tong, S. Yue, et al., “Tailored Environment-Friendly Reverse Type-I Colloidal Quantum Dots for a Near-Infrared Optical Synapse and Artificial Vision System,” *ACS Nano* 18 (2024): 29991–30003.

68. H. Yang, Y. Hu, X. Zhang, et al., “Near-Infrared Optical Synapses Based on Multilayer $MoSe_2$ Moiré Superlattice for Artificial Retina,” *Advanced Functional Materials* 34 (2024): 2308149.

69. J. Sung, S. W. Kim, D. Lee, et al., “Co-Stimuli-Driven 2D WSe_2 Optoelectronic Synapses for Neuromorphic Computing,” *Small* 21 (2025): 2504024.

70. T. Zhang, C. Fan, L. Hu, et al., “A Reconfigurable All-Optical-Controlled Synaptic Device for Neuromorphic Computing Applications,” *ACS Nano* 18 (2024): 16236–16247.

71. C. Qian, S. Oh, Y. Choi, et al., “Solar-Stimulated Optoelectronic Synapse Based on Organic Heterojunction With Linearly Potentiated Synaptic Weight for Neuromorphic Computing,” *Nano Energy* 66 (2019): 104095.

72. P. Fang, W. He, Y. Lin, et al., “A Synaptic Transistor Based on van der Waals Heterojunction $HfS_2/HfO_x/SnS_2$ With Optical Modulation Properties,” *Applied Physics Letters* 124 (2024): 173104.

73. C. Chen, Q. Sun, Y. Lu, et al., “X-Ray Irradiation Improved WSe_2 Optical–Electrical Synapse for Handwritten Digit Recognition,” *Nanomaterials* 15 (2025): 1408.

74. X.-Z. Zhang, R.-Z. Luo, and J. Chen, “Revisit the Poynting Vector in PT-Symmetric Coupled Waveguides,” *Optics Express* 30 (2022): 38753.

75. W. Ji, L. Zhang, and W. Xie, “Improving Efficiency Roll-Off in Phosphorescent OLEDs by Modifying the Exciton Lifetime,” *Optics Letters* 37 (2012): 2019.

76. L. Zhang, H. Jiang, T. Huang, et al., “Ag-LSPR and Molecular Additive: A Collaborative Approach to Improve the Photovoltaic Performance of Perovskite Solar Cells,” *Chemical Engineering Journal* 481 (2024): 148572.

77. P. Qin, T. Wu, Z. Wang, et al., “Grain Boundary and Interface Passivation With Core–Shell Au@CdS Nanospheres for High-Efficiency Perovskite Solar Cells,” *Advanced Functional Materials* 30 (2020): 1908408.

78. Y. Xie, W. Zhou, J. Yin, et al., “Post-Annealing to Recover the Reduced Open-Circuit Voltage Caused by Solvent Annealing in Organic Solar Cells,” *Journal of Materials Chemistry A* 4 (2016): 6158–6166.

79. W. Wang, S. Gao, Y. Li, et al., “Artificial Optoelectronic Synapses Based on $TiNxO_{2-x}/MoS_2$ Heterojunction for Neuromorphic Computing and Visual System,” *Advanced Functional Materials* 31 (2021): 2101201.

80. T. Chang, S.-H. Jo, and W. Lu, “Short-Term Memory to Long-Term Memory Transition in a Nanoscale Memristor,” *ACS Nano* 5 (2011): 7669–7676.

81. H. Tan, Q. Tao, I. Pande, et al., “Tactile Sensory Coding and Learning With Bio-Inspired Optoelectronic Spiking Afferent Nerves,” *Nature Communications* 11 (2020): 1369.

82. Y. Zhou, J. Fu, Z. Chen, et al., “Computational Event-Driven Vision Sensors for In-Sensor Spiking Neural Networks,” *Nature Electronics* 6 (2023): 870–878.

Supporting Information

Additional supporting information can be found online in the Supporting Information section.

Supporting File 1: agt270319-sup-0001-SuppMat.docx.

26924560, 2026, 3, Downloaded from https://onlinelibrary.wiley.com/doi/10.1002/agt2.70319 by HONG KONG POLYTECHNIC UNIVERSITY HU NG HOM, Wiley Online Library on [10/04/2026]. See the Terms and Conditions (https://onlinelibrary.wiley.com/terms-and-conditions) on Wiley Online Library for rules of use; OA articles are governed by the applicable Creative Commons License